INTERFACE

rsif.royalsocietypublishing.org

Research

Cite this article: Wangpraseurt D, Wentzel C, Jacques SL, Wagner M, Kühl M. 2017 *In vivo* imaging of coral tissue and skeleton with optical coherence tomography. *J. R. Soc. Interface* **14**: 20161003.
http://dx.doi.org/10.1098/rsif.2016.1003

Received: 11 December 2016
Accepted: 1 February 2017

Subject Category:
Life Sciences–Earth Science interface

Subject Areas:
bioenergetics, bioengineering, environmental science

Keywords:
optical coherence tomography, coral tissue, microstructure, bioimaging, green fluorescent protein

Authors for correspondence:
Daniel Wangpraseurt
e-mail: dw527@cam.ac.uk
Michael Kühl
e-mail: mkuhl@bio.ku.dk

†Present address: Department of Chemistry, University of Cambridge, Lensfield Road, Cambridge, UK.

Electronic supplementary material is available online at https://dx.doi.org/10.6084/m9.figshare.c.3691885.

THE ROYAL SOCIETY PUBLISHING

In vivo imaging of coral tissue and skeleton with optical coherence tomography

Daniel Wangpraseurt[1,†], Camilla Wentzel[1], Steven L. Jacques[2], Michael Wagner[3] and Michael Kühl[1,4]

[1]Marine Biological Section, Department of Biology, University of Copenhagen, Strandpromenaden 5, Helsingør 3000, Denmark
[2]Department of Biomedical Engineering, Oregon Health and Science University, 3303 SW Bond Avenue, Portland, OR 97239, USA
[3]Engler-Bunte Institute, Chair of Water Chemistry and Water Technology, Karlsruhe Institute of Technology, Engler-Bunte-Ring 1, 76131 Karlsruhe, Germany
[4]Climate Change Cluster, University of Technology Sydney, PO Box 123, Broadway, Sydney, New South Wales 2007, Australia

DW, 0000-0003-4834-8981; MK, 0000-0002-1792-4790

Application of optical coherence tomography (OCT) for *in vivo* imaging of tissue and skeleton structure of intact living corals enabled the non-invasive visualization of coral tissue layers (endoderm versus ectoderm), skeletal cavities and special structures such as mesenterial filaments and mucus release from intact living corals. Coral host chromatophores containing green fluorescent protein-like pigment granules appeared hyper-reflective to near-infrared radiation allowing for excellent optical contrast in OCT and a rapid characterization of chromatophore size, distribution and abundance. *In vivo* tissue plasticity could be quantified by the linear contraction velocity of coral tissues upon illumination resulting in dynamic changes in the live coral tissue surface area, which varied by a factor of 2 between the contracted and expanded state of a coral. Our study provides a novel view on the *in vivo* organization of coral tissue and skeleton and highlights the importance of microstructural dynamics for coral ecophysiology.

1. Introduction

Coral reefs are hotspots of biodiversity and one of the most productive ecosystems on the Earth [1]. The key drivers of this productive ecosystem are reef building (scleractinic) corals, i.e. invertebrates that belong to the family Cnidaria that live in symbiotic interaction with dinoflagellate microalgae of the genus *Symbiodinium*. Coral reefs are characterized by a rich structural complexity as coral colonies grow in diverse shapes such as branch-like, hemispherical, encrusting or plate-like morphotypes [2]. The structure of coral skeletons has been studied in detail from macroscopic colony scales down to the nanometre scale, where scanning electron microscopy, three-dimensional laser scanning and X-ray microcomputed tomography have acquired high-resolution structural information of coral skeletons [3–5], which has significantly advanced our understanding of coral structure and calcification [6]. Coral skeletons are primarily composed of aragonite (i.e. $CaCO_3$). Coral skeleton microstructure has also been shown to modulate the backscattering of light [7], which can affect the light exposure of *Symbiodinium* in the coral tissue [8]. It has been suggested that such skeleton-derived differences in backscatter can explain differences among corals in their susceptibility to bleaching under environmental stress [9].

Much less is known about the structural complexity of intact living corals, albeit coral tissue and its plasticity, that is the ability to contract/expand and re-arrange itself over the skeleton matrix, evidently must play an important role for coral ecophysiology. The exchange of solutes and metabolites is controlled

at the coral tissue–water interface and is a function of the interaction between water flow and coral tissue topography [10,11]. Coral tissue microtopography affects the thickness of the diffusive boundary layer, that is the thin layer of water covering the coral tissues where diffusion is the prime transport mechanism, which can be rate limiting for respiration and photosynthesis [12]. The buildup of a thermal boundary layer controls the heat exchange of corals and is likewise affected by flow and tissue surface topography [13]. Additionally, coral tissue properties strongly modulate the optical microenvironment of coral photosymbiotic microalgae known as zooxanthellae, where, for example, tissue thickness and opacity control *Symbiodinium* light exposure via formation of distinct light gradients [14] that are further affected by the presence and distribution of coral host pigments, such as the green fluorescent protein (GFP) containing chromatophore system [15,16].

The morphological properties of coral tissues are not static, and corals can re-arrange their tissues within seconds in response to the ambient light environment [17,18], changes in the concentration of gases [10] and water movement as well as food exposure [19]. Both the thermal and optical microenvironments of *Symbiodinium* are affected by tissue contraction or expansion [16,17]. Together, the structural and optical properties of the coral tissue and its plasticity in terms of distribution over the coral skeleton strongly modulate coral photosynthesis, respiration and the exchange of solutes with the surrounding seawater [20], and there is a need for non-invasive *in vivo* imaging techniques that can resolve tissue structural dynamics on the micrometre scale and in real time for individual coral polyps.

Descriptions of coral tissue structure have largely been based on light microscopy [21,22], histological sectioning and electron microscopy, which requires extensive tissue sample preparation that can introduce artefacts such as tissue shrinkage and dehydration. Microscopic imaging of live intact corals has also been realized in the laboratory [23,24] and *in situ* [25] but information about internal tissue organization is limited to early developmental stages, tissue explants or corals with thin tissue layers without pronounced calcified structures. Depth resolution and contrast in light microscopy is hampered by the absorption and scattering of visible light in the tissue–skeleton matrix, and the same effects limit the depth resolution of confocal laser scanning microscopy on coral tissue to the outermost 100–200 µm using high numerical aperture objective lenses with a small field of view [26]. Recently, digital holographic microscopy (DHM) was used for non-invasive imaging of mucus formation in cold-water corals [27]. DHM is a novel, essentially lens-free phase imaging method based on recording the interference between visible light passing through the sample and a reference light beam, where the interference pattern of an imaged object is first stored as a digital hologram and then digitally processed with reconstruction algorithms [27]. While DHM can provide fast and non-invasive imaging of coral surfaces and (semi-)transparent surface layers such as mucus, its depth penetration is expected to be lower than in optical coherence tomography (OCT) for dense, scattering media such as coral tissue and skeleton.

Biomedical tissue imaging faces similar challenges as listed above for coral tissues, and several spectroscopic imaging techniques have been developed, where the use of near-infrared radiation (NIR) bears distinct advantages for non-invasive structural imaging in terms of greater penetration depth, field of view coverage and image acquisition speed [28]. A key NIR-based technique that has revolutionized dermatology and ophthalmology is OCT [29] that allows for non-invasive *in vivo* cross-sectional characterization of tissues with an imaging penetration depth of several millimetres and with micrometre resolution. OCT measures characteristic patterns of directly elastically backscattered (low coherent ballistic and near ballistic) photons from different reflective layers in a sample, e.g. at refractive index mismatches between tissue compartments with different microstructural properties [30]. Signal contrast in OCT thus depends on the optical scattering properties of the investigated material, where light scattering creates good image contrast, while highly NIR absorbing media result in poor images. Recently, OCT imaging has been applied in the environmental sciences in order to understand the structure and function of biofilms [31], higher plants [32] and aquatic vertebrates [33]. In this study, we explored the use of OCT for studying coral tissue microstructure and dynamics. We demonstrate that OCT can be used as a rapid, non-invasive coral imaging technique that can easily be implemented in experimental set-ups to gain high resolution tomographic data on coral skeleton and tissue structure, and we present novel OCT-based approaches for the *in vivo* characterization of a GFP-like chromatophore system, coral mucus, tissue movement and surface area in living corals.

2. Results and discussion

2.1. Basic microstructural features of coral tissues

OCT was well suited for studying the structure of tissues and skeleton of intact living corals *in vivo*, where the use of NIR avoided any PAR-related effects on the coral host or photosymbionts (e.g. tissue movement [18]). The tissues of all investigated coral, spanning a wide range of morphologies and tissue thickness, could be imaged with excellent optical contrast (figure 1). Recently, it has been shown that coral tissues exhibit strong light scattering [16,17] with scattering coefficients similar to human and plant tissues [16,17,34]. Therefore, OCT was ideally suited to resolve microstructural features of coral tissues (figures 1 and 2).

Close-up OCT scans of the oral disc of the massive thick-tissued coral *Favites abdita* revealed a highly heterogeneous coral tissue surface with tissue lobes surrounding the immediate mouth opening (figure 2*a–d*). OCT B-scans revealed the oral ectoderm which was approximately 90 µm thick followed by a thin (approx. 50 µm layer) of low OCT signal which likely relates to the mesoglea (figure 2*d*; electronic supplementary material, figure S1). The oral endoderm was also visible and at least 30 µm thick (electronic supplementary material, figure S1). Along the A-scan axis beyond the oral endoderm, the OCT signal was quickly attenuated and imaging penetration depth was around 500 µm from the coral tissue surface. Thus for the thick-tissued *F. abdita*, the OCT imaging was limited to the upper tissue layers (figure 2*b*,*d*).

By contrast, imaging of the thin-tissued *Acropora aspera* generated higher axial penetration depths of up to 1 mm, visualizing the entire coral tissue and the underlying skeleton (figure 2*e–g*). The coral tissue of *A. aspera* appeared as one continuous tissue layer due to the steady linear attenuation of the OCT signal along the A-scan axis within the coral tissue (figure 2*d*; electronic supplementary material, figure S1). OCT signal attenuation within *A. aspera* was lower compared with

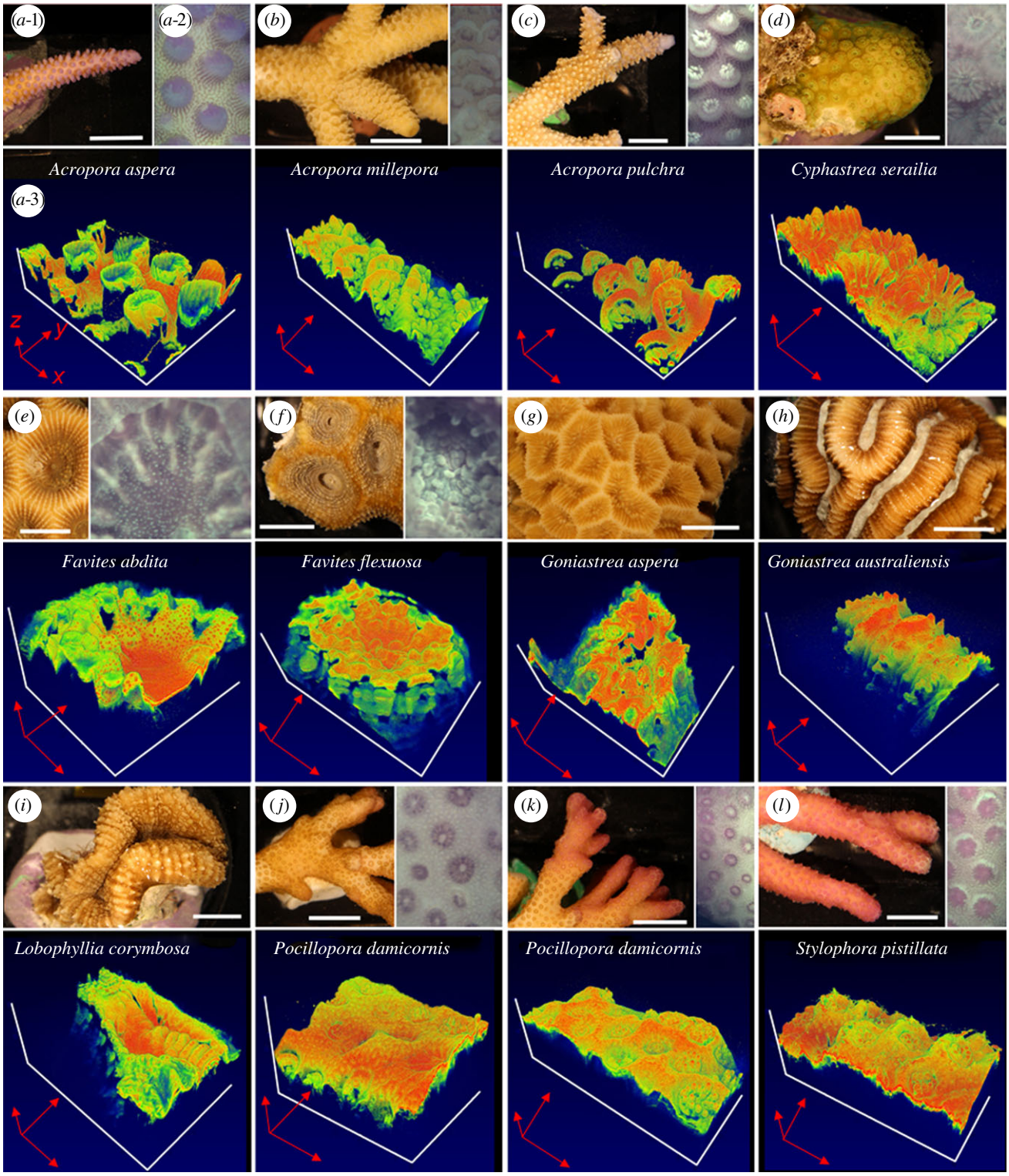

Figure 1. (*a*–*l*) Three-dimensional OCT imaging of coral microtopographic diversity (*a*-1). Macrostructure of an *Acropora aspera* branch (white scale bar, 1 cm). (*a*-2) Close-up, top view of *Acropora aspera* tissue microstructure photographed with the USB camera of the OCT system. The photographed tissue surface area corresponds to the area imaged with OCT shown in panel (*a*-3). The three-dimensional OCT scan is shown in *x*-,*y*-,*z*-dimensions. Red arrows are 2 mm in length for *x*,*y* and 1 mm in length for the *z*-dimension. The false colour coding represents the intensity of the uncalibrated OCT signal, which was manually adjusted to optimize visualization of structural features for each scan (see Material and methods for details). Note that panel number labelling is only shown for panel (*a*) (for clarity) and that no USB camera image was taken for some coral species as OCT scanning was performed in darkness to ensure tissue relaxation.

F. abdita, which allowed for imaging the aragonite skeleton below the animal tissue layer (figure 2*e*,*g*). The OCT scans further revealed that the tissue was connected to the skeleton via channel-like 'pillars' that were on average 20–50 µm in diameter (see 'c' in figure 2*g*). Scanning electron microscopy of dead coral skeletons showed the presence of such skeletal extrusions of 40–100 µm width in *A. aspera* [35]. OCT now allows for imaging the tissue–skeleton interface of live corals without the need for tissue removal and/or decalcification, thus facilitating the *in vivo* investigation of skeletal structures and growth, e.g. through repeated monitoring of defined tissue and skeleton section of the same individual [6]. Additionally, OCT can also be used to only image the exposed skeleton with good optical contrast (electronic supplementary material,

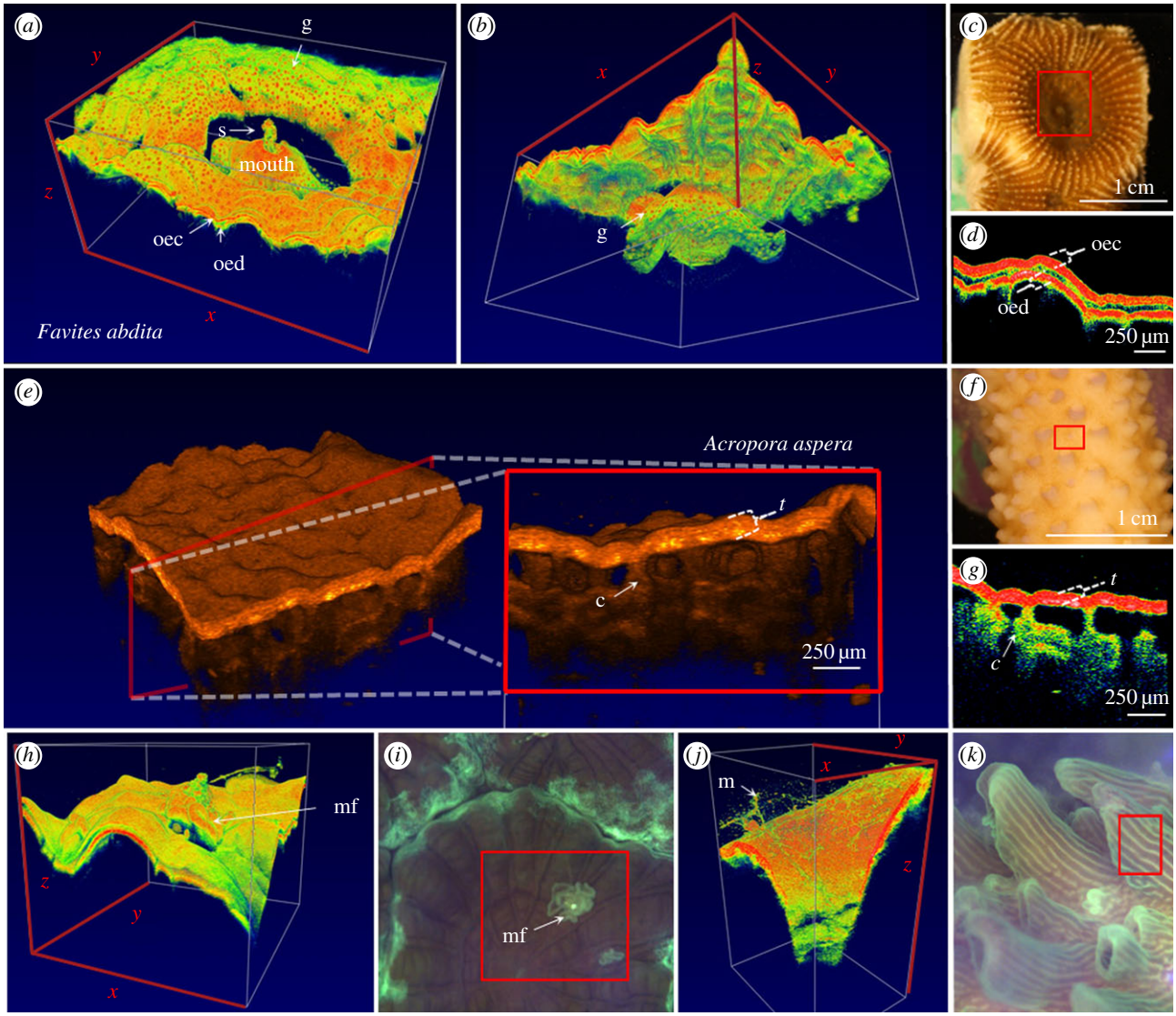

Figure 2. Microstructural imaging of coral tissues using OCT. (*a–d*) *Favites abdita*. (*a*) Three-dimensional rendering of a single polyp. The rendering visualizes the convoluted surface topography and polyp mouth and identifies the oral ectoderm (oec), the oral endoderm (oed), GFP granule containing chromatophores (g) as well as sediment ingestion (s). (*b*) Rear view of (*a*). The field of view of the OCT scan was $x = 5.25$ mm, $y = 4.4$ mm and $z = 2.8$ mm. Video animation of the three-dimensional rendering can be found in electronic supplementary material, movie S1. (*c*) Image of coral polyp. The red square illustrates the approximate area imaged with OCT. (*d*) Close-up view of tissue arrangement in cross-sectional OCT B-scan mode. (*e–g*) *Acropora aspera*. (*e*) Three-dimensional inlet shows representative *en face* plane of a coenosarc area. The scan identifies the entire tissue (t) and skeletal channels (c). (*f*) Photograph of live coral, red square shows approximate OCT scan area, (*g*) close-up view showing the channel-like structures. (*h*) Three-dimensional rendering of mesenterial filaments (mf) based on imaged area (red square) in (*i*) ($x = 3.0$, $y = 3.4$, $z = 2.8$ mm). (*j*) Three-dimensional rendering of coral mucus (m) based on imaged area (red square) in (*k*) ($x = 1.1$, $y = 1.45$, $z = 2.8$ mm). A video animation of coral mucus movement can be found in the electronic supplementary material, movie S2. False colour coding blue to red (highest signal in red) and orange tones (highest signal in brightest tones) was manually adjusted to optimize image contrast.

figure S3) and might thus provide a suitable alternative to, for example, a three-dimensional laser scanner [5].

Assuming an anisotropy of scattering factor g of approximately 0.9 and a coral tissue scattering coefficient μ_s of approximately 100 cm^{-1} in dense Faviid polyp tissue [34], we would expect a depth limit for OCT imaging of approximately 300–500 µm (see Material and methods), which fits our experimental observations in *F. abdita* (figure 1; electronic supplementary material, figure S1). The operational OCT imaging depth was larger in Acroporids and other branched corals, which might reflect a lower scattering coefficient and/or lower overall attenuation of the 930 nm OCT probing light in such thin-tissued corals. A more precise quantification of how different corals and different coral structures affect the operational depth of OCT awaits further quantification of the inherent optical properties of corals [34].

2.2. Imaging coral tissue and mucus dynamics

Research in coral reef science has been dominated by studies on the response of corals to environmental stress including global warming, ocean acidification, pollution and diseases [36,37]. OCT imaging can facilitate the early detection of ecophysiological stress through microscale visualization of behavioural modifications *in vivo*. For instance, mesenterial filaments can be expelled from the polyp stomach and extruded to the coral surface in response to temperature stress [21] and space competition with neighbouring corals and predators [38]. A recently developed underwater microscope was able to record mesenterial filament extrusion at high spatial and temporal resolution [25]. Likewise, OCT was capable of following and visualizing the extrusion of such filaments through temporary openings with microscale spatial resolution (figure 2*h–i*). The good visibility of mesenterial

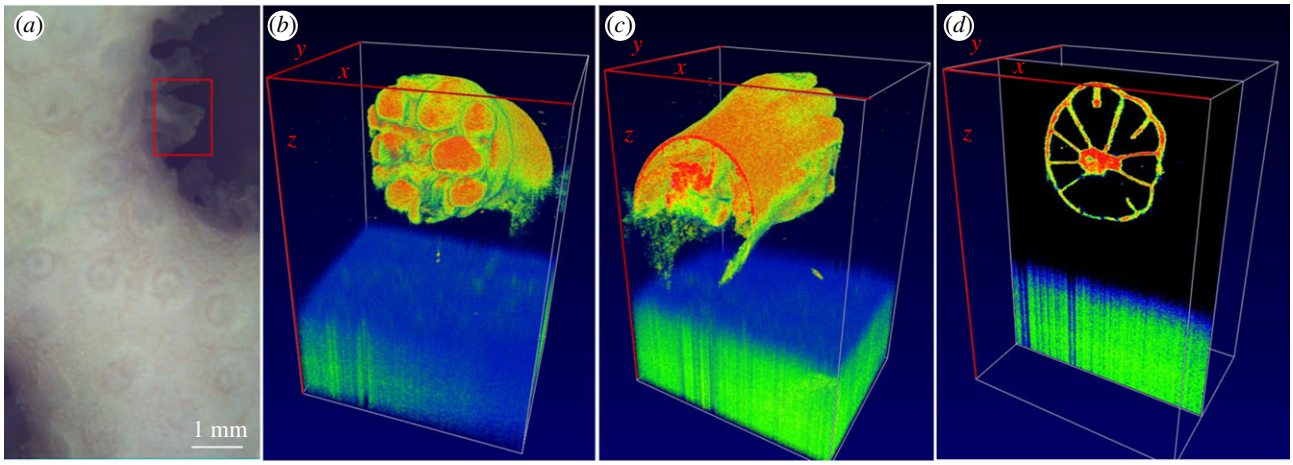

Figure 3. OCT imaging of a single bleached coral polyp. (*a*) The image shows the bleached surface of the coral *Pocillopora damicornis*. The red square corresponds to the area scanned with OCT. (*b*,*c*) Three-dimensional rendered coral in volume view and (*d*) in sectional view. The field of view of the OCT scan was $x = 1.2$ mm, $y = 9.45$ mm and $z = 2.8$ mm.

filaments is likely related to their considerable (yet unquantified) amount of lipid reserves [21] creating a sufficiently strong refractive index mismatch with the surrounding medium to result in excellent contrast and visualization through OCT (figure 2*h*).

Coral mucus is fundamental to the exchange of energy on coral reefs, and mucus can contain 20–45% of the photosynthetically fixed carbon of corals [39]. Mucus excretion is affected by, for example, temperature and light stress, bacterial infection, particle sedimentation and coral exposure to air [40]. There has been substantial interest in imaging and quantifying coral mucus, but visualization has been hampered as it is almost invisible in conventional light microscopy, and mucus quantification has thus mainly relied on volumetric bulk measurements [41]. Mucus is essentially a hydrated gel [40] and quantification via histology suffers from artefacts during sample preparation due to dehydration and subsequent shrinkage. DHM was recently used for visualizing the *in vivo* mucus secretion in cold-water corals [27] and this novel technique seems well suited for similar studies on symbiont-bearing corals. Here we show that OCT is a suitable alternative to DHM as it was able to resolve the string and sheath-like mucus structures adhering to the coral surface (figure 2*j*,*k*; electronic supplementary material, figure S2). By exposing the coral *A. aspera* to air for about 30 s, we were able to stimulate excessive mucus production. Owing to the rapid data acquisition of OCT, mucus excretion and transport can now be quantified and followed in real time (electronic supplementary material, figure S2 and movie S2).

The OCT is not a suitable tool to image microalgal loss during coral bleaching (figure 3). The optical properties of *Symbiodinium* are dominated by light absorption [8], although microalgal cells do also scatter light [42]. We imaged a bleached polyp of the coral *Pocillopora damicornis*, revealing no major differences in the OCT signal generated from the polyp as compared to healthy tissues (figure 3*a*–*d*). Sectioning of the coral polyp revealed clearly the stomach tissues of the polyp (figure 3*d*). The good visibility of coral tissues independent of *Symbiodinium* density suggests that OCT can be used to detect early sublethal signs of environmental stress such as changes in tissue thickness prior to coral bleaching [43]. Hitherto, changes in coral microstructure upon temperature stress have primarily been assessed with invasive imaging techniques that require tissue sectioning such as conventional light microscopy or scanning electron microscopy [43]. By contrast, the non-invasive OCT approach now allows rapid and repeated *in vivo* monitoring for early signs of stress responses in intact corals.

2.3. Visualization of coral host pigments

The coral animal host has several potential means to protect its photosymbionts from excess radiative stress that can otherwise cause photoinhibition [44]. The coral animal synthesizes various fluorescent [45] and non-fluorescent pigments [46] as well as myscosporine-like amino acids [47]. GFP-like host pigments are homologous to the well-known green fluorescent proteins that are widely used as fluorescent markers in life sciences. There thus exists a major body of research dealing with the structure and function of GFP-like pigments in corals (e.g. [26,45,48]). In coral science, much effort has been dedicated to reveal the function of GFP-like pigments for coral photosynthesis. It has been shown that they can be photoprotective and might thus play an important role in the resilience of corals to climate change related coral bleaching [15]. However, it is suggested that the photoprotective function of GFP depends on the distance of GFP to the photosymbiotic algae, the density of GFP-like pigments within the tissue and the structural arrangement of the proteins [15,16,44]. GFP-like pigments can occur in pigment granules (approx. 1 µm in size) that can aggregate to a dense chromatophore system or it can be homogeneously incorporated in the animal tissue [15,49]. *In vivo* visualization of GFP-like host pigment granules has been achieved by confocal laser scanning microscopy using their natural fluorescence to create image contrast [15]. However, in addition to their fluorescent properties, GFP-like pigments are also highly scattering [16]. In this study, we demonstrated that OCT is able to distinguish and identify chromatophores containing GFP-like host pigment granules with good contrast from the remaining coral tissue, due to their strong light scattering properties causing strong OCT signals (figures 4*a*–*c* and 5).

For the investigated *F. abdita* coral, GFP chromatophores were exclusively located in the upper ectoderm (figure 4*a*,*b*), where the density of GFP chromatophores within the coral

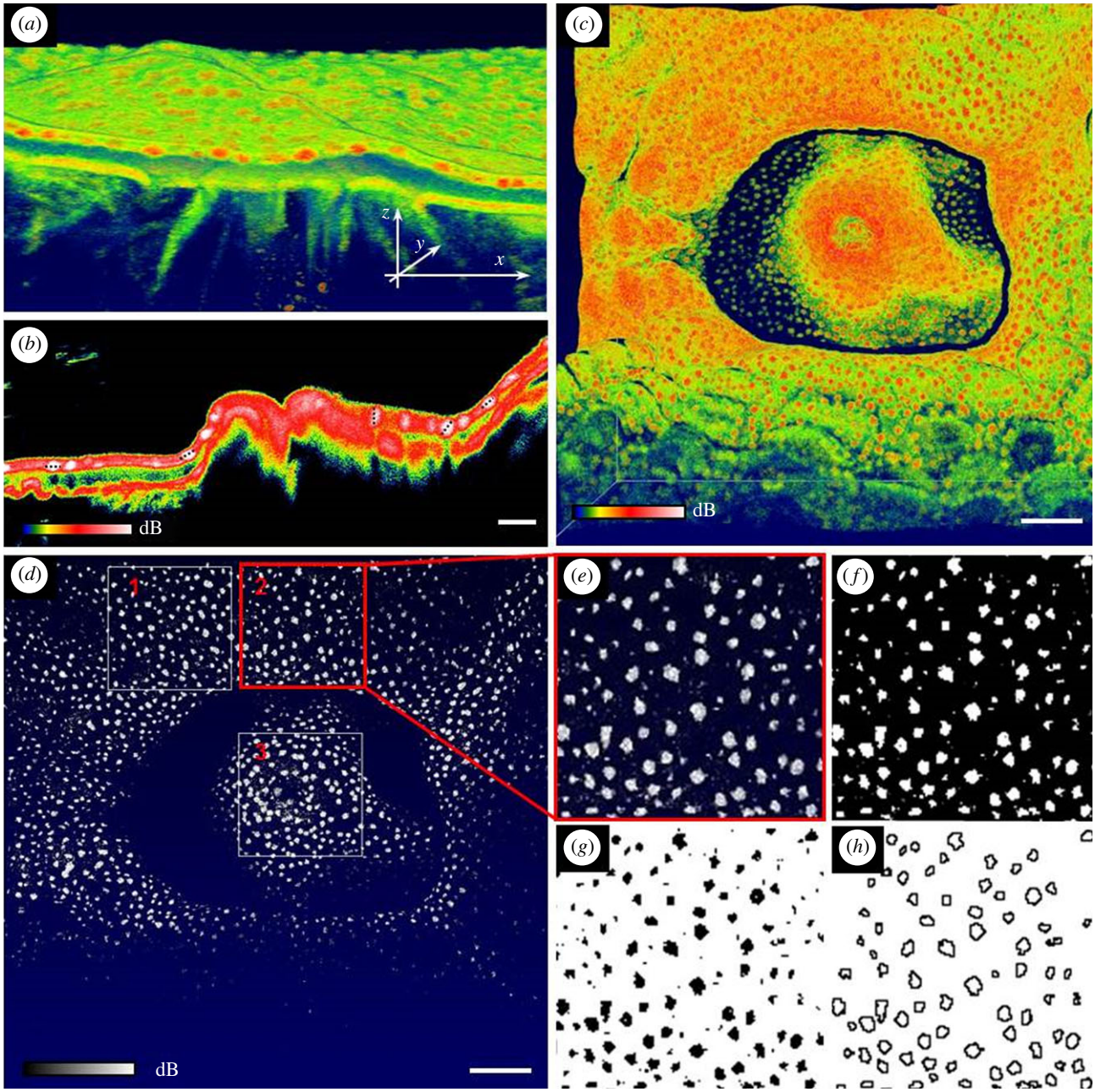

Figure 4. Imaging and segmentation of GFP containing chromatophore system. (*a*) Close-up of a three-dimensional rendering of the *Favites abita* polyp shown in figure 1*e*. Highest OCT signal intensity (in red) reveals chromatophores. Length of arrows equals 500 µm. (*b*) Cross-sectional OCT B-scan through the polyp mouth. Chromatophore visualization (in white) was enhanced through narrowing the threshold of the OCT signal. Dotted black lines show examples of maximum chromatophore diameter. Scale bar, 100 µm (*c*). Top view of three-dimensional rendering of coral polyp in false colour mode and (*d*) in black and white colour mode. Scale bar, 500 µm. Regions of interest (labelled 1–3) of 1 mm^2 quadrats were selected for chromatophore analysis. (*e–h*) Example of segmentation steps to yield physical characteristics of chromatophores. (*e*) Close-up of region of interest 2, (*f*) brightness and contrast adjusted image, (*g*) binarized image using the Otsu algorithm and (*d*) detected particles (see Material and methods for details).

polyp tissues was on average 97 ($\pm$15) granules mm^{-2} of projected two dimensional surface area, which translated to a surface cover of 13% ($\pm$4%) within the imaged polyp tissue. The maximal diameter of the chromatophores was on average 85 ($\pm$13.8) µm as assessed through OCT B-scanning. Size–frequency distributions calculated a median chromatophore size of $1.0–1.5 \times 10^3$ μm^2 per projected surface area (figure 4). Previous studies have characterized GFP granules and reported on the existence of the chromatophore system [15,50], but a quantification of the abundance and size structure of chromatophores over larger coral tissue areas has hitherto been lacking. Photomicrographs of thin histological sections shown in Schlichter *et al*. [49] revealed the presence of chromatophores about 60 µm in diameter. Likewise, confocal microscopy stacks showed the presence of chromatophores within the same size category (approx. 50–100 µm) [15]. Thus although there is no comparable size distribution estimate on the reported chromatophore system, our OCT-based size estimates fall within the range reported in the earlier studies. While OCT is a good method to rapidly assess the basic properties and *in vivo* abundance of chromatophores within larger tissue areas without the need for physical preparation, more diffusely incorporated GFP pigments were not clearly discernible and the two morphotypes of *P. damicornis* (brown, non-fluorescent versus pink, fluorescent) did not reveal characteristic differences in their OCT signal (figure 1*j*,*k*).

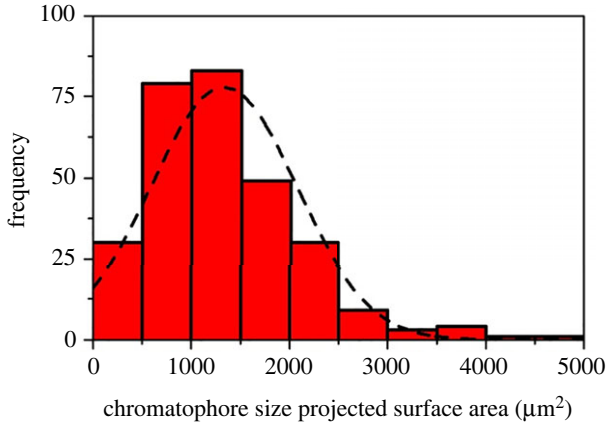

Figure 5. Size–frequency distribution of GFP containing chromatophore system of *Favites abdita*. Chromatophore size is calculated in relation to the projected two-dimensional surface area (square micrometre). Chromatophore identification is based on image analysis shown in figure 4. (Online version in colour.)

2.4. Coral tissue movement

Although corals appear to be static on the macroscale, coral tissues are flexible on the micrometre to centimetre scale, where coral tissues can re-arrange on the scale of seconds due to, for example, physical force, behavioural control or illumination [25]. Massive thick-tissued corals respond to excess illumination via tissue contraction [18], which can increase tissue surface reflectivity and affect the internal tissue light microenvironment [17]. However, a precise quantification of such tissue plasticity has been lacking. We, therefore, traced the linear velocity of tissue contraction by acquiring a series of OCT B-scans at a high frame rate (figure 6). Upon illumination, a *F. abdita* polyp accelerated within 3–5 s to a maximum linear tissue movement velocity of approximately 120 $\mu m\, s^{-1}$, whereafter the velocity decreased linearly until movement stopped within approximately 20 s. In the current example, we captured B-scans of 4 mm wide × 2.8 mm deep vertical sections of intact coral tissue and skeleton at a frame rate of 0.7 s (electronic supplementary material, movie S3). Reducing the spatial resolution and field of view to dedicated areas would even enable coral movements to be followed at video rate resolution [51].

Gas exchange is regulated across the tissue–water interface and thus partially controlled by the area of exposed tissue surface [20,52]. Corals thus have the capacity to alter gas exchange dynamics through significantly changing their exposed surface area. *Symbiodinium* light exposure will also be affected by changes in tissue contraction and expansion [17]. Surface area is thus an important metric in coral biology research, where metabolic rates and, for example, *Symbiodinium* cell numbers are often normalized to coral surface area. Coral surface area has mainly been estimated from coral skeleton architecture through, for example, wax dipping and foil wrapping techniques or X-ray scanning based computer tomography [53]. Direct surface area quantification on intact corals has also been attempted with photogrammetry [53–55], but these techniques have been established for surface area characterization on centimetre and metre scales, largely neglecting the micro-architectural complexity and plasticity of coral tissue surfaces (figure 1). Changes in tissue surface structure are likely to affect tissue surface and subsurface scattering as well as the optical path length between coral tissue surface and *Symbiodinium*. OCT provides a method to quantify such dynamic changes in surface structure and tissue density. Here we developed an OCT-based method to rapidly quantify coral surface area for a given tissue state (see 'Image analysis' in Material and methods section). We calculated the change in three-dimensional tissue surface area of the coral *P. damicornis* upon tissue contraction (figure 7) as the ratio of the three-dimensional surface area normalized to the two-dimensional projected surface area. Our calculations showed an approximate doubling (2.14 times) of relative tissue surface area upon tissue expansion from 2.2 (contracted) to 4.5 times (expanded) in the coral *P. damicornis*. This illustrates the importance of taking such dynamic changes in tissue structure into account, e.g. when normalizing rates of photosynthesis or respiration to coral surface area.

In conclusion, our study (i) introduces OCT to coral research, (ii) demonstrates a novel view on the *in vivo* organization of coral tissue and skeleton, and (iii) highlights the importance of quantifying microstructural dynamics for coral ecophysiology. Coral tissue and skeleton microstructure was imaged with excellent optical contrast, and OCT further allowed for the characterization of coral tissue surface area, distribution and abundance of GFP-like pigment granules, and quantification of coral tissue contraction at a hitherto unreached spatio-temporal resolution on living corals. OCT is also well suited for monitoring early responses of corals to environmental stress in the form of mucus excretion and mesenterial filament extrusion. This first application of OCT in coral reef science also points to several future developments. For instance, biomedical OCT analysis has developed image analysis algorithms that allow for advanced image correction for optical artefacts such as speckle noise, as well as for dedicated segmentation of microstructural features [56], and implementation and optimization of such tools for coral OCT analysis seems promising. The same holds true for the use of calibrated OCT measurements for extracting inherent optical properties [57] such as the scattering coefficient of coral tissue and skeleton. Commercial OCT systems are compact, portable and robust and can easily be incorporated into typical experimental set-ups for ecophysiological studies of corals. Inclusion of OCT in such studies can provide key information about coral structure, such as *in vivo* quantification of tissue surface area dynamics under different experimental treatments. This novel approach may also be highly relevant and applicable for structural *in vivo* studies in other aquatic organisms and systems.

3. Material and methods

3.1. Optical coherence tomography system and measuring principle

We used a commercially available spectral-domain (SD) OCT system (Ganymede II, Thorlabs GmbH, Dachau, Germany) equipped with an objective lens with an effective focal length of 36 mm, and a working distance of 25.1 mm (LSM03; Thorlabs GmbH, Dachau, Germany; figure 1*a*). The OCT system includes a superluminescent diode (SLD) emitting broadband low coherent light centred at 930 nm. The light source sets a limit to the axial resolution of OCT imaging defined as the so-called coherence length or gate [58]:

$$\Delta z = \frac{2\ln 2}{n\pi}\frac{\lambda^2}{\Delta\lambda}, \tag{3.1}$$

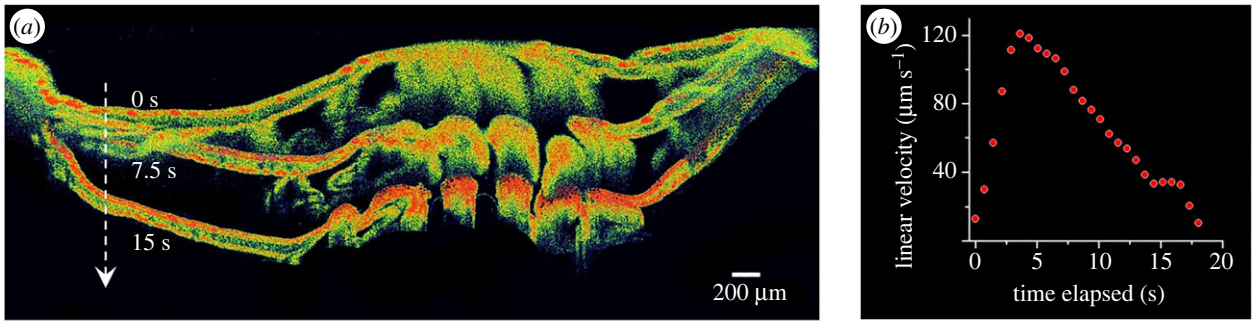

Figure 6. *In vivo* cross-sectional tracking of tissue movement. (*a*) Sequence of OCT B-scans (false colour mode) performed after illuminating the coral *Favites abdita*. The three scans show the coral polyp in an expanded state in darkness (0 s) and after 7.5 s and 15 s of high light illumination. The three images are superimposed for visualizing tissue plasticity (see electronic supplementary material, movie S3 for real-time video of tissue contraction). (*b*) Estimated maximal linear velocity of tissue movement calculated as the running average of the vertical displacement of a white marker (see Material and methods section) towards the centre of the image over three frames (about 2.2 s).

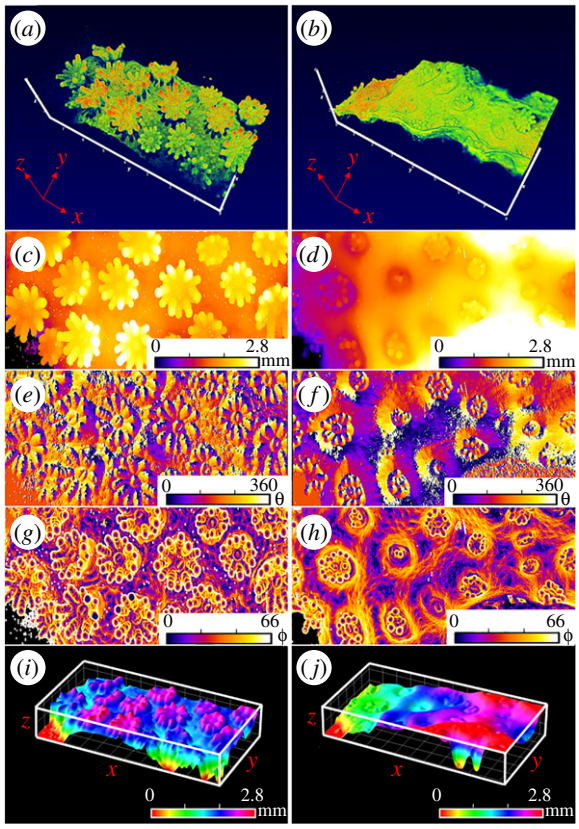

Figure 7. OCT-based surface area characterization of expanded (*a*,*c*,*e*,*g*,*i*) versus contracted coral tissue (*b*,*d*,*f*,*h*,*j*). (*a*,*b*) Three-dimensional OCT scan (*x*,*y*,*z* scale bar, 1 mm). (*c*,*d*) Topographic height map ($z = 0-2.8$ mm in false colour coding). (*e*,*f*) The gradient analysis (see Material and methods section) calculated the azimuthal angle θ showing the surface direction from 0° to 360°, and (*g*,*h*) the polar angle ϕ showing the surface orientation from 0° to 66°. (*i*,*j*) The reconstructed three-dimensional tissue surface (see Material and methods section). The surface height *z* is shown in false colour coding for $z = 0-2.8$ mm. The field of view of the OCT scans was $x = 3.4$ mm, $y = 7.7$ mm and $z = 2.8$ mm.

where n is the refractive index of the medium ($n = 1.33$ for water), λ is the centre wavelength ($\lambda = 930$ nm) and $\Delta\lambda$ is the full width at half maximum of the power spectrum of the SLD ($\Delta\lambda = 65$ nm). Thus in our case Δz was 4.5 µm. By contrast, the lateral resolution is dependent on the imaging optics, which in our system generated a limit to the x–y resolution of 8 µm.

The light generated by the SLD is coupled into a bifurcated fibre which is connected to the OCT imaging probe (electronic supplementary material, figure S4). The key components of the imaging probe consist of a beam splitter, a galvano-optical system (galvanometer and mirror), a retro-reflecting prism and a charged coupled device detector (electronic supplementary material, figure S4). The OCT system is additionally equipped with a USB camera and LED ring that facilitates observation of the samples and definition of the OCT scan direction/area.

The operating principle of OCT is based on white light interferometry similar to a Michelson type interferometer [58] (electronic supplementary material, figure S4), where broadband low coherent light from the SLD is split by a beam splitter into two partially coherent beams, a reference beam and a sample beam. The sample beam penetrates the object along the *z*-axis, while the reference light is reflected by a retro-reflecting mirror within the imaging probe. In a one-dimensional A-scan, the sample beam interacts with the coral tissue and light is reflected from different microstructural features along the *z*-axis. The locally reflected light is collected and combined with the reference beam, generating a characteristic interference pattern. In time-domain OCT, the reference mirror is rapidly scanned along the *z*-axis in order to vary the optical path length and thus imaging a particular depth of interest. In SD OCT, which was applied here, no mechanical scanning of the reference arm is needed and instead the cross-spectral density is measured by a spectrometer that characterizes the unique phase delay of each wavelength, which significantly improves the imaging speed of the OCT system. An A-scan's interferometric signal from each (*x*,*y*) position is converted into a signal of reflectance as a function of depth (*z*) with 4.5 µm maximal axial resolution, which allows separation of the different coral tissue layers and skeleton scatter [34]. To generate two-dimensional transects (B-scans) and three-dimensional stacks of transect (C-scans), a galvanometer system inside the imaging probe moves the A-scan sample beam along the *x*- and *y*-axis. The built-in USB camera in the OCT scan head enabled us to define exact scan positions, transects and areas relative to the visible coral structure.

The vertical penetration depth and image contrast for the employed OCT system are affected by the NIR (930 nm) attenuation, primarily due to absorption in water [58] and multiple scattering in coral tissue and skeleton [14,34]. The OCT signal originates from directly backscattered photons, while multiple scattering reduces image resolution and contrast with increasing sampling depth. The operational limit for the OCT imaging penetration depth is affected by the scattering mean free path, i.e. the inverse of the reduced scattering coefficient μ_s'. The reduced scattering coefficient is defined as

$$\mu_s' = \mu_s(1 - g), \tag{3.2}$$

where μ_s is the scattering coefficient and g is the anisotropy of scattering, i.e. a measure of the directionality of the scattering [58]. Most biological tissues are highly forward scattering ($g = 0.9$) [59] and the operational penetration depth of OCT imaging typically is approximately three to five times the scattering mean free path [58].

The SD OCT system used here allows for video rate scanning, with a maximal A-scan rate of 36 kHz given there is sufficient contrast in the sampled OCT signal. Conventionally, the SD OCT data are described as a signal-to-noise ratio (in decibel, dB). The generated SD OCT data represent a relative measure of the locally backscattered light and carry quantitative optical information that can be used to calculate the scattering coefficient of a biological tissue [57]. However, the characterization of tissue optical properties necessitates a careful calibration of the OCT detector optics and measuring set-up. Such OCT calibration involves correcting for a potential signal drop off along the z-axis and the focus function of the objective lens. Calibration of the OCT data in absolute units, i.e. reflected power, is rarely performed in OCT studies, where the primary aim is the visualization of structural features [31]. In this study, the OCT data are thus shown in dB and visualization was aided through false colour coding and grey scaling of the OCT dB signal (see below for details).

3.2. Sampling of corals

Sun-adapted corals were collected from shallow waters (less than 2 m depth) on the reef flat of Heron Island, Great Barrier Reef, Australia (152°06′ E, 20°29′ S). Fragments of the corals *Acropora millepora*, *A. aspera*, *A. pulchra*, *Cyphastrea serailia*, *F. abdita*, *F. flexuosa*, *Goniastrea aspera*, *Lobophyllia corymbosa*, *Goniastrea australiensis*, *P. damicornis* (brown and pink morph) and *Stylophora pistillata* were selected; coral identification was done according to Veron [60]. The coral species were chosen to cover a wide range of different surface structures and skeletal architectures as well as different types of tissue thickness and pigmentation, e.g. due to the presence of GFP-like coral host pigments. After collection, colonies were fragmented into smaller pieces of a few square centimetres in size, mounted onto microscope slides and photo documented. All corals were kept under natural light conditions in outdoor aquaria at the Heron Island research station supplied with a constant flow of fresh seawater.

3.3. Optical coherence tomography imaging set-up

Coral OCT measurements were done indoors under defined light conditions provided by a fibre-optic halogen lamp (KL-2500LCD, Schott GmbH, Germany) with individual coral samples positioned in a custom-made black acrylic flow chamber connected to a 10 l water reservoir with fresh aerated seawater [14]. The flow velocity was about 0.5 cm s^{-1} with a constant water temperature of approximately 24°C and a salinity of 33–35. To optimize the signal to noise ratio in the measurements, the corals were positioned within the flow chamber such that only a small amount of water (less than 3 mm) was on top of the coral surface, which minimized water absorption of the 930 nm sample light beam; thinner water layers resulted in optical artefacts due to air–water reflections. It was also important to minimize flow chamber vibrations, which otherwise led to interference artefacts in the OCT scans.

Measurements on intact corals were performed by selecting a region of interest (ROI) using the image generated by the USB camera of the OCT system. The USB camera image was first brought into focus using the manual focusing stage. The reference arm length was then adjusted until the OCT signal was maximized within the uppermost 30% of the image field [61]. OCT scanning was performed in B-scan (cross-sectional) and C-scan (three-dimensional, series of B-scans) mode using an A-scan averaging of at least 10 scans with an A-scan rate of 36 kHz. Fast measurements of single B-scans were also performed to follow dynamic changes in coral tissue structure due to light-induced tissue contraction [17]. For this, a *F. abdita* fragment was kept in darkness in order to lead to a complete relaxation of the oral polyp tissue, which could be followed by OCT scanning in darkness. The polyp was then illuminated by a fibre optic tungsten halogen lamp (see above) providing a downwelling photon irradiance (PAR, 400–700 nm) of $E_d = 3000$ µmol photons m^{-2} s^{-1}, while the tissue contraction was followed in OCT B-scan timeframe mode, recording subsequent B-scans at a frame rate of 0.7 s. Additionally, we tested the suitability of OCT to image the exposed skeleton by removing the coral tissue with an air-gun and repeating OCT measurements under the same underwater conditions. For coral skeleton imaging, it was important to release any air trapped between skeleton ridges upon immersion by carefully tapping the skeleton and brushing its surface underwater with a paintbrush.

3.4. Image analysis

Visualization of OCT B- and C-scans was done with the manufacturer's imaging software (ThorImage 4.2; Thorlabs GmbH, Dachau, Germany) using the in-built brightness and contrast functions. The images were visualized assuming a constant refractive index of water ($n = 1.33$). The refractive index scales the image and thus affects any length and velocity estimates. OCT C-scans were saved as 'raw + processed' data in the software and were then converted to 32-bit grayscale multiple tiff image stacks using a custom-made macro written in ImageJ [31]. Post-processing was performed in a Fiji installation of ImageJ [62] as described below.

A protocol was developed for the non-invasive characterization of GFP chromatophore abundance and size by OCT, as preliminary observations revealed that OCT is capable of imaging and identifying the highly reflective chromatophores of GFP-like host pigments in the coral *F. abdita* [16]. For this, OCT C-scans were rendered in ThorImage 4.2, and a manual contrast adjustment was performed in monochrome modus to maximize the OCT dB signal contrast between GFP chromatophores and the surrounding tissue. The rendered OCT three-dimensional scan was exported as a JPG image with a z-axis orientation of 0° (i.e. top view) and imported into ImageJ. For the investigated coral polyps, OCT B-scans revealed that the chromatophores were exclusively located as a single layer of granules within the upper oral tissue layer allowing for a particle density estimate based on a single rendered JPG file.

Three 1 mm^2 ROI were manually selected within image areas that showed maximal signal/noise ratios. For each ROI image, brightness and contrast were adjusted, followed by conversion to 8-bit and binarization via the Otsu segmentation algorithm [63] plugin in ImageJ. The Otsu automatic thresholding algorithm minimizes the intra-class variance between black and white pixels [63] while ensuring no significant loss of granule features. The binarized image was then analysed for granule density using the ImageJ automated particle analyser plugin. Granule detection was optimized through size boundaries ($pixels^2 = 7.5 - \infty$) and hole filling, while the image edges were excluded. The particle analyser calculated the chromatophore number per projected surface area, chromatophore size (in micrometre projected surface area), as well as the per cent surface cover by chromatophores. Additionally, the average maximal diameter of GFP chromatophores was estimated from OCT B-scans, i.e. tissue cross sections, using the manual thresholding function of ThorImage v. 4.2.

The linear velocity of coral tissue contraction was calculated from recorded time-series of B-scans using an automated single-particle tracking algorithm, TrackmateJ [64]. The frame sequence was first exported from ThorImage 4.2 in RGB mode and converted to 8-bit grey scale images in ImageJ. For each frame, a white circle (diameter = 25 pixels) was added adjacent to the tissue surface to aid in boundary detection (electronic

supplementary material, movie S3). The tissue surface contraction was tracked in the constant speed tracking mode of TrackmateJ using an estimated blob diameter of 100 pixels and a threshold of 2 [64]. The maximal linear velocity was calculated in micrometres per second as the running average of the vertical displacement over three subsequent frames (approx. 2.2 s) for each frame.

The coral tissue surface rendering and surface area analysis involved image thresholding and binarization, development of a topographic height map followed by a gradient analysis. Extracted OCT C-scans (32-bit grayscale tiff image stacks) were first adjusted for image brightness and contrast following conversion to 8-bit in ImageJ. The stacks were then binarized using the Otsu automatic thresholding algorithm (see above). Subsequently, remaining noise, i.e. white pixels not related to the coral surface, was removed using the remove outlier function of ImageJ. The images were cropped such that maximal tissue surface height equaled $z = 0$. A depth-coding algorithm [31] then converted the binarized tiff image stacks to a continuous height function $z(x,y)$, where each z value was assigned a pseudo colour-coded pixel value equal to the distance from $z = 0$. The generated height map was visualized as a two-dimensional surface plot in order to reconstruct the surface topography of the OCT C-scan.

The surface area of the reconstructed surface topography was then calculated using SurfCharJ, an ImageJ plugin originally developed for paper structure analysis [65]. SurfCharJ estimates surface roughness and surface area by performing a gradient analysis that measures the intensity and orientation of local surface structures of the topographic image. The orientation of a surface in three-dimensional space can be described by the direction of the outward surface normal vector, $\hat{n}$[68]. In polar coordinates, $\hat{n}$ is given in terms of the polar angle, θ, and the azimuthal angle, ϕ, by

$$\hat{n} = n_x\hat{x} + n_y\hat{y} + n_z\hat{z} = (\hat{x}\cos\varphi + \hat{y}\sin\varphi)\sin\theta + \hat{z}\cos\theta, \quad (3.3)$$

where $\hat{x}$, $\hat{y}$ and $\hat{z}$ are unit vectors of the, respective, axes. The topographic height data relate to the coordinate angles (θ, ϕ) by

$$\phi = \arctan\left(\frac{\frac{\partial z}{\partial y}}{\frac{\partial z}{\partial x}}\right) \quad \text{and} \quad \theta_{xy} = \arctan\sqrt{\left(\frac{\partial z}{\partial x}\right)^2 + \left(\frac{\partial z}{\partial y}\right)^2}, \quad (3.4)$$

where z is the surface height. Equations (3.3) and (3.4) show how the angles are related to the gradients of the height data in the topographic map. The gradients are then estimated using a series of imaging processing algorithms that are described in further detail in Chinga *et al*. [65]. Briefly, the gradient analysis calculates the orientation of the local surface relative to the coral surface, i.e. the polar image, and the direction of the local surfaces relative to the coral tissue plane, i.e. the azimuthal image. The coral tissue surface area (SA) is then calculated based on the gradient analysis as

$$\begin{aligned} \mathrm{SA} &= \int_s \mathrm{d}A \iint \sqrt{1 + \left(\frac{\partial z}{\partial x}\right)^2 + \left(\frac{\partial z}{\partial y}\right)^2 + \mathrm{d}x\,\mathrm{d}y} \\ &= \iint \sqrt{1 + \tan^2\theta}\,\mathrm{d}x\,\mathrm{d}y \\ &\approx \sum_{i=1}^{N_x}\sum_{j=1}^{N_y} \sqrt{1 + \tan^2\theta_{ij}}. \end{aligned} \quad (3.5)$$

The coral tissue surface area could thus be calculated as the ratio between the actual coral tissue surface area (in square micrometres) relative to the planar area imaged with OCT (in square micrometres).

Data accessibility. All data supporting the findings of this study are available within the article and the electronic supplementary material. Original OCT raw data are available from the corresponding authors upon request.

Authors' contributions. D.W. and M.K. designed the study. D.W. and C.W. performed measurements. S.L.J. and M.W. provided analytical tools. D.W. analysed data with input from S.L.J., M.W. and M.K. D.W. and M.K. wrote the article with editorial input from all co-authors.

Competing interests. The authors declare that the research was conducted in the absence of any commercial or financial relationships that could be construed as a potential conflict of interest.

Funding. This study was funded by a Carlsberg Foundation Distinguished Postdoctoral Fellowship (D.W.), a Carlsberg Foundation instrument grant (M.K.) and a Sapere Aude advanced grant from the Danish Council for Independent Research/Natural Sciences (M.K.).

Acknowledgements. We acknowledge Sofie Lindegaard Jakobsen, Erik Trampe and the staff at Heron Island research station for help and technical assistance during fieldwork. Ingrun Schönberg and Jörg Wollenzin (Thorlabs GmbH, Luebeck, Germany) are thanked for technical advice on OCT system operation.

References

1. Hatcher BG. 1990 Coral reef primary productivity. A hierarchy of pattern and process. *Trends Ecol. Evol.* **5**, 149–155. (doi:10.1016/0169-5347(90)90221-X)
2. Kaandorp JA, Kübler JE. 2001 *The algorithmic beauty of seaweeds, sponges and corals*. Berlin, Germany: Springer.
3. Stolarski J. 2003 Three-dimensional micro- and nanostructural characteristics of the scleractinian coral skeleton: a biocalcification proxy. *Acta Palaeontol. Pol.* **48**, 497–530.
4. Meibom A, Cuif J-P, Houlbreque F, Mostefaoui S, Dauphin Y, Meibom KL, Dunbar R. 2008 Compositional variations at ultra-structure length scales in coral skeleton. *Geochim. Cosmochim. Acta* **72**, 1555–1569. (doi:10.1016/j.gca.2008.01.009)
5. Raz-Bahat M, Faibish H, Mass T, Rinkevich B. 2009 Three-dimensional laser scanning as an efficient tool for coral surface area measurements. *Limnol. Oceanogr. Methods* **7**, 657–663. (doi:10.4319/lom.2009.7.657)
6. Tambutté E, Allemand D, Zoccola D, Meibom A, Lotto S, Caminiti N, Tambutté S. 2007 Observations of the tissue-skeleton interface in the scleractinian coral *Stylophora pistillata*. *Coral Reefs* **26**, 517–529. (doi:10.1007/s00338-007-0263-5)
7. Marcelino LA *et al.* 2013 Modulation of light enhancement to symbiotic algae by light-scattering in corals and evolutionary trends in bleaching. *PLoS ONE* **8**, e61492. (doi:10.1371/journal.pone.0061492)
8. Teran E, Mendez ER, Enriquez S, Iglesias-Prieto R. 2010 Multiple light scattering and absorption in reef-building corals. *Appl. Opt.* **49**, 5032–5042. (doi:10.1364/AO.49.005032)
9. Swain TD *et al.* 2016 Skeletal light-scattering accelerates bleaching response in reef-building corals. *BMC Ecol.* **16**, 10. (doi:10.1186/s12898-016-0061-4)
10. Kühl M, Cohen Y, Dalsgaard T, Jørgensen BB, Revsbech NP. 1995 Microenvironment and photosynthesis of zooxanthellae in scleractinian corals studied with microsensors for O_2, pH and light. *Mar. Ecol. Prog. Ser.* **117**, 159–172. (doi:10.3354/meps117159)
11. Wangpraseurt D, Weber M, Roy H, Polerecky L, de Beer D, Suharsono, Nugues MM. 2012 *In situ* oxygen dynamics in coral-algal interactions. *PLoS ONE* **7**, e31192. (doi:10.1371/journal.pone.0031192)
12. Jorgensen BB, Revsbech NP. 1985 Diffusive boundary layers and the oxygen uptake of sediments and detritus. *Limnol. Oceanogr.* **30**, 111–122. (doi:10.4319/lo.1985.30.1.0111)
13. Jimenez IM, Kuhl M, Larkum AWD, Ralph PJ. 2011 Effects of flow and colony morphology on the

thermal boundary layer of corals. *J. R. Soc. Interface* **8**, 1785–1795. (doi:10.1098/rsif.2011.0144)

14. Wangpraseurt D, Larkum AW, Ralph PJ, Kühl M. 2012 Light gradients and optical microniches in coral tissues. *Front. Microbiol*. **3**, 316. (doi:10.3389/fmicb.2012.00316)
15. Salih A, Larkum A, Cox G, Kühl M, Hoegh-Guldberg O. 2000 Fluorescent pigments in corals are photoprotective. *Nature* **408**, 850–853. (doi:10.1038/35048564)
16. Lyndby NH, Kühl M, Wangpraseurt D. 2016 Heat generation and light scattering of green fluorescent protein-like pigments in coral tissue. *Sci. Rep*. **6**, 26599. (doi:10.1038/srep26599)
17. Wangpraseurt D, Larkum AW, Franklin J, Szabó M, Ralph PJ, Kühl M. 2014 Lateral light transfer ensures efficient resource distribution in symbiont-bearing corals. *J. Exp. Biol*. **217**, 489–498. (doi:10.1242/jeb.091116)
18. Levy O, Dubinsky Z, Achituv Y. 2003 Photobehavior of stony corals: responses to light spectra and intensity. *J. Exp. Biol*. **206**, 4041–4049. (doi:10.1242/jeb.00622).
19. Sebens K, Johnson A. 1991 Effects of water movement on prey capture and distribution of reef corals. *Hydrobiologia* **226**, 91–101. (doi:10.1007/BF00006810)
20. Patterson MR. 1992 A chemical engineering view of cnidarian symbioses. *Am. Zool*. **32**, 566–582. (doi:10.1093/icb/32.4.566)
21. Brown B, Le Tissier M, Bythell J. 1995 Mechanisms of bleaching deduced from histological studies of reef corals sampled during a natural bleaching event. *Mar. Biol*. **122**, 655–663. (doi:10.1007/BF00350687)
22. Hayes R, Bush P. 1990 Microscopic observations of recovery in the reef-building scleractinian coral, *Montastrea annularis*, after bleaching on a Cayman reef. *Coral Reefs* **8**, 203–209. (doi:10.1007/BF00265012)
23. Sivaguru M, Fried GA, Miller CA, Fouke BW. 2014 Multimodal optical microscopy methods reveal polyp tissue morphology and structure in Caribbean reef building corals. *J. Vis. Exp.* **91**, e51824. (doi:10.3791/51824)
24. Shapiro OH, Kramarsky-Winter E, Gavish AR, Stocker R, Vardi A. 2016 A coral-on-a-chip microfluidic platform enabling live-imaging microscopy of reef-building corals. *Nat. Commun*. **7**, 10860. (doi:10.1038/ncomms10860)
25. Mullen AD, Treibitz T, Roberts PL, Kelly EL, Horwitz R, Smith JE, Jaffe JS. 2016 Underwater microscopy for *in situ* studies of benthic ecosystems. *Nat. Commun*. **7**, 12093. (doi:10.1038/ncomms12093)
26. Salih A. 2012 Screening reef corals for novel GFP-type fluorescent proteins by confocal imaging. *Methods Mol. Biol*. **872**, 217–233. (doi:10.1007/978-1-61779-797-2_15)
27. Zetsche E-M, Baussant T, Meysman FJ, van Oevelen D. 2016 Direct visualization of mucus production by the cold-water coral *Lophelia pertusa* with digital holographic microscopy. *PLoS ONE* **11**, e0146766. (doi:10.1371/journal.pone.0146766)
28. Vogler N, Heuke S, Bocklitz TW, Schmitt M, Popp J. 2015 Multimodal imaging spectroscopy of tissue. *Annu. Rev. Anal. Chem*. **8**, 359–387. (doi:10.1146/annurev-anchem-071114-040352)
29. Huang D *et al.* 1991 Optical coherence tomography. *Science* **254**, 1178–1181. (doi:10.1126/science.1957169)
30. Schmitt JM. 1999 Optical coherence tomography (OCT): a review. *IEEE J. Sel. Top. Quantum Electron*. **5**, 1205–1215. (doi:10.1109/2944.796348)
31. Wagner M, Taherzadeh D, Haisch C, Horn H. 2010 Investigation of the mesoscale structure and volumetric features of biofilms using optical coherence tomography. *Biotechnol. Bioeng.* **107**, 844–853. (doi:10.1002/bit.22864)
32. Hettinger JW *et al.* 2000 Optical coherence microscopy. A technology for rapid, *in vivo*, non-destructive visualization of plants and plant cells. *Plant Physiol*. **123**, 3–16. (doi:10.1104/pp.123.1.3)
33. Speiser DI, Gagnon YL, Chhetri RK, Oldenburg AL, Johnsen S. 2016 Examining the effects of chromatic aberration, object distance, and eye shape on image-formation in the mirror-based eyes of the bay scallop *Argopecten irradians*. *Integr. Comp. Biol.* **56**, 834–841. (doi:10.1093/icb/icw099)
34. Wangpraseurt D, Jacques S, Petri T, Kuhl M. 2016 Monte Carlo modeling of photon propagation reveals highly scattering coral tissue. *Front. Plant Sci*. **7**, 1404. (doi:10.3389/fpls.2016.01404)
35. Brown B, Sya'Rani L, Le Tissier M. 1985 Skeletal form and growth in *Acropora aspera* (Dana) from the Pulau Seribu, Indonesia. *J. Exp. Mar. Biol. Ecol*. **86**, 139–150. (doi:10.1016/0022-0981(85)90027-9)
36. Hughes TP *et al.* 2003 Climate change, human impacts, and the resilience of coral reefs. *Science* **301**, 929–933. (doi:10.1126/science.1085046)
37. Hoegh-Guldberg O *et al.* 2007 Coral reefs under rapid climate change and ocean acidification. *Science* **318**, 1737–1742. (doi:10.1126/science.1152509)
38. Nugues MM, Delvoye L, Bak RPM. 2004 Coral defence against macroalgae: differential effects of mesenterial filaments on the green alga *Halimeda opuntia*. *Mar. Ecol. Prog. Ser*. **278**, 103–114. (doi:10.3354/meps278103)
39. Wild C, Huettel M, Klueter A, Kremb SG, Rasheed MY, Jørgensen BB. 2004 Coral mucus functions as an energy carrier and particle trap in the reef ecosystem. *Nature* **428**, 66–70. (doi:10.1038/nature02344)
40. Brown B, Bythell J. 2005 Perspectives on mucus secretion in reef corals. *Mar. Ecol. Prog. Ser*. **296**, 291–309. (doi:10.3354/meps296291)
41. Jatkar AA, Brown BE, Bythell JC, Guppy R, Morris NJ, Pearson JP. 2010 Measuring mucus thickness in reef corals using a technique devised for vertebrate applications. *Mar. Biol*. **157**, 261–267. (doi:10.1007/s00227-009-1313-z)
42. Morel A, Bricaud A. 1986 Inherent optical properties of algal cells including picoplankton: theoretical and experimental results. *Can. Bull. Fish. Aquat. Sci*. **214**, 521–559.
43. Ainsworth T, Hoegh-Guldberg O, Heron S, Skirving W, Leggat W. 2008 Early cellular changes are indicators of pre-bleaching thermal stress in the coral host. *J. Exp. Mar. Biol. Ecol*. **364**, 63–71. (doi:10.1016/j.jembe.2008.06.032)
44. Baird AH, Bhagooli R, Ralph PJ, Takahashi S. 2009 Coral bleaching: the role of the host. *Trends Ecol. Evol*. **24**, 16–20. (doi:10.1016/j.tree.2008.09.005)
45. Alieva NO *et al.* 2008 Diversity and evolution of coral fluorescent proteins. *PLoS ONE* **3**, e2680. (doi:10.1371/journal.pone.0002680)
46. Dove SG, Lovell C, Fine M, Deckenback J, Hoegh-Guldberg OVE, Iglesias-Prieto R, Anthony KRN. 2008 Host pigments: potential facilitators of photosynthesis in coral symbioses. *Plant Cell Environ*. **31**, 1523–1533. (doi:10.1111/j.1365-3040.2008.01852.x)
47. Shick JM, Dunlap WC. 2002 Mycosporine-like amino acids and related gadusols: biosynthesis, accumulation, and UV-protective functions in aquatic organisms. *Annu. Rev. Physiol*. **64**, 223–262. (doi:10.1146/annurev.physiol.64.081501.155802)
48. Oswald F *et al.* 2007 Contributions of host and symbiont pigments to the coloration of reef corals. *FEBS J.* **274**, 1102–1109. (doi:10.1111/j.1742-4658.2007.05661.x)
49. Schlichter D, Meier U, Fricke H. 1994 Improvement of photosynthesis in zooxanthellate corals by autofluorescent chromatophores. *Oecologia* **99**, 124–131. (doi:10.1007/BF00317092)
50. Schlichter D, Weber W, Fricke H. 1985 A chromatophore system in the hermatypic, deep-water coral *Leptoseris fragilis* (Anthozoa: Hexacorallia). *Mar. Biol*. **89**, 143–147. (doi:10.1007/BF00392885)
51. Blauert F, Horn H, Wagner M. 2015 Time-resolved biofilm deformation measurements using optical coherence tomography. *Biotechnol. Bioeng*. **112**, 1893–1905. (doi:10.1002/bit.25590)
52. Patterson MR, Sebens KP. 1989 Forced convection modulates gas exchange in cnidarians. *Proc. Natl Acad. Sci. USA* **86**, 8833–8836. (doi:10.1073/pnas.86.22.8833)
53. Naumann MS, Niggl W, Laforsch C, Glaser C, Wild C. 2009 Coral surface area quantification—evaluation of established techniques by comparison with computer tomography. *Coral Reefs* **28**, 109–117. (doi:10.1007/s00338-008-0459-3)
54. Courtney LA, Fisher WS, Raimondo S, Oliver LM, Davis WP. 2007 Estimating 3-dimensional colony surface area of field corals. *J. Exp. Mar. Biol. Ecol*. **351**, 234–242. (doi:10.1016/j.jembe.2007.06.021)
55. Holmes G. 2008 Estimating three-dimensional surface areas on coral reefs. *J. Exp. Mar. Biol. Ecol*. **365**, 67–73. (doi:10.1016/j.jembe.2008.07.045)
56. Kafieh R, Rabbani H, Kermani S. 2013 A review of algorithms for segmentation of optical coherence tomography from retina. *J. Med. Signals Sens*. **3**, 45–60.

57. Levitz D, Thrane L, Frosz M, Andersen P, Andersen C, Andersson-Engels S, Valanciunaite J, Swartling J, Hansen P. 2004 Determination of optical scattering properties of highly-scattering media in optical coherence tomography images. *Opt. Express* **12**, 249–259. (doi:10.1364/OPEX.12.000249)
58. Fercher AF, Drexler W, Hitzenberger CK, Lasser T. 2003 Optical coherence tomography-principles and applications. *Rep. Prog. Phys*. **66**, 239. (doi:10.1088/0034-4885/66/2/204)
59. Jacques SL. 2013 Optical properties of biological tissues: a review. *Phys. Med. Biol*. **58**, R37. (doi:10.1088/0031-9155/58/11/R37)
60. Veron JEN. 2000 *Corals of the world*, vols 1–3. Townsville, Australia: Australian Institute of Marine Science.
61. Yaqoob Z, Wu J, Yang C. 2005 Spectral domain optical coherence tomography: a better OCT imaging strategy. *Biotechniques* **39**, 6–13. (doi:10.2144/000112090)
62. Schindelin J *et al.* 2012 Fiji: an open-source platform for biological-image analysis. *Nat. Methods* **9**, 676–682. (doi:10.1038/nmeth.2019)
63. Zhang J, Hu J. 2008 Image segmentation based on 2D Otsu method with histogram analysis. In *IEEE Int. Conf. on Computer Science and Software Engineering, Wuhann, China, 12–14 December 2008*, vol. 6, pp. 105–108. (doi:10.1109/CSSE.2008.206)
64. Tinevez J-Y, Perry N, Schindelin J, Hoopes GM, Reynolds GD, Laplantine E, Bednarek SY, Shorte SL, Eliceiri KW. In press. TrackMate: an open and extensible platform for single-particle tracking. *Methods*. (doi:10.1016/j.ymeth.2016.09.016)
65. Chinga G, Johnsen PO, Dougherty R, Berli EL, Walter J. 2007 Quantification of the 3D microstructure of SC surfaces. *J. Microsc*. **227**, 254–265. (doi:10.1111/j.1365-2818.2007.01809.x)